

CrossZoom: Simultaneously Motion Deblurring and Event Super-Resolving

Chi Zhang, Xiang Zhang, Mingyuan Lin, Cheng Li, Chu He, Wen Yang, Gui-Song Xia, Lei Yu

Abstract—Even though the collaboration between traditional and neuromorphic event cameras brings prosperity to frame-event based vision applications, the performance is still confined by the resolution gap crossing two modalities in both spatial and temporal domains. This paper is devoted to bridging the gap by increasing the temporal resolution for images, *i.e.*, motion deblurring, and the spatial resolution for events, *i.e.*, event super-resolving, respectively. To this end, we introduce CrossZoom, a novel unified neural Network (CZ-Net) to jointly recover sharp latent sequences within the exposure period of a blurry input and the corresponding High-Resolution (HR) events. Specifically, we present a multi-scale blur-event fusion architecture that leverages the scale-variant properties and effectively fuses cross-modality information to achieve cross-enhancement. Attention-based adaptive enhancement and cross-interaction prediction modules are devised to alleviate the distortions inherent in Low-Resolution (LR) events and enhance the final results through the prior blur-event complementary information. Furthermore, we propose a new dataset containing HR *sharp-blurry* images and the corresponding HR-LR event streams to facilitate future research. Extensive qualitative and quantitative experiments on synthetic and real-world datasets demonstrate the effectiveness and robustness of the proposed method. Codes and datasets are released at <https://bestrivenzcg.github.io/CZ-Net/>.

Index Terms—Motion Deblurring, Event Super-Resolving, Low-Resolution Events, Cross Enhancement

INTRODUCTION

NUMEROUS frame-event fusion-based approaches have been developed for diverse applications [10], [15], [37], [43], [45], capitalizing on the complementary spatiotemporal characteristics between conventional and event cameras. On the one hand, Event-assisted methods for Intensity image enhancement, *i.e.*, the E4I approaches [15], [39], commonly extract the inter/intra-frame information in terms of textures and motions as a complement benefiting from extremely high temporal resolution while disregarding their inherent limited spatial resolution [12], [16], [34]. On the other hand, conventional intensity images are often considered as the guidance to denoise and super-resolve the noisy Low-Resolution (LR) event streams leading to the I4E approaches [37], [45]. However, motion blurs in dynamic scenes often result in a significant loss in temporal resolution and are typically overlooked in I4E approaches. The prevalent cross-modality inconsistency in the spatial resolution and occurrence of motion blur in degraded image frames (particularly in dynamic scenes with fast-moving objects) severely impair the performance [16], [34], [37], [45].

Despite the considerable advances in both E4I and I4E, limited exploration has been dedicated to simultaneously considering prevalent spatial resolution inconsistency and motion blur [10], [41]. To boost the application of frame-event fusion-based approaches, a pressing need is emerging to simultaneously restore High-Resolution (HR) event streams and sharp images from a single HR blurry image and concurrent LR events, as shown in Fig. 1. Although one can achieve this by applying a two-stage cascaded approach that employs Event Super-Resolving (ESR) methods for LR events to assist existing Event-based Motion Deblurring (EMD) approaches, such a cascaded scheme often leads to sub-optimal performance since the deblurring or super-resolution errors will be propagated to the subsequent stage and inevitably degenerate the overall performance, as shown in Fig. 1 (b).

Hence, we propose a unified architecture to accomplish the two tasks simultaneously, although its implementation is non-trivial. Specifically, the feasibility of this architecture is underpinned by the complementarity between HR blurry images and LR events. HR blurry images still contain valuable HR texture information capable of guiding ESR tasks [11], while the LR events encompass intra-frame motion and texture information that mitigate motion ambiguity in MD tasks. Nonetheless, this scheme introduces coupled distortions that increase the complexity of the task, *i.e.*, coupled distortions primarily consist of motion ambiguity and texture erasure within the blurry image, as well as noise and texture discontinuity in the LR events arising from spatial degradation, as shown in Fig. 1 (e). These intertwined complexities significantly intensify the ill-posedness of the MD and ESR tasks within a unified framework. Thus, the crucial challenge in architecting this unified cross-task scheme becomes evident: *effectively mitigating coupled*

- C. Zhang, M. Lin, C. He, W. Yang, and L. Yu are with the School of Electronic Information, Wuhan University, Wuhan 430072, China. E-mail: {zhangchi1, linmingyuan, chuhe, yangwen, ly.wd}@whu.edu.cn.
- X. Zhang is with the Computer Vision Lab of ETH Zurich, Switzerland. E-mail: xiang.zhang@vision.ee.ethz.ch.
- C. Li is with the Huawei Noah's Ark Lab, Shenzhen, China. E-mail: licheng89@huawei.com.
- G. S. Xia is with the School of Computer Science, Wuhan University, Wuhan 430072, China. E-mail: guisong.xia@whu.edu.cn.
- The research was partially supported by the National Natural Science Foundation of China under Grants 62271354, 62523111, and 61871297.
- Corresponding author: Lei Yu.

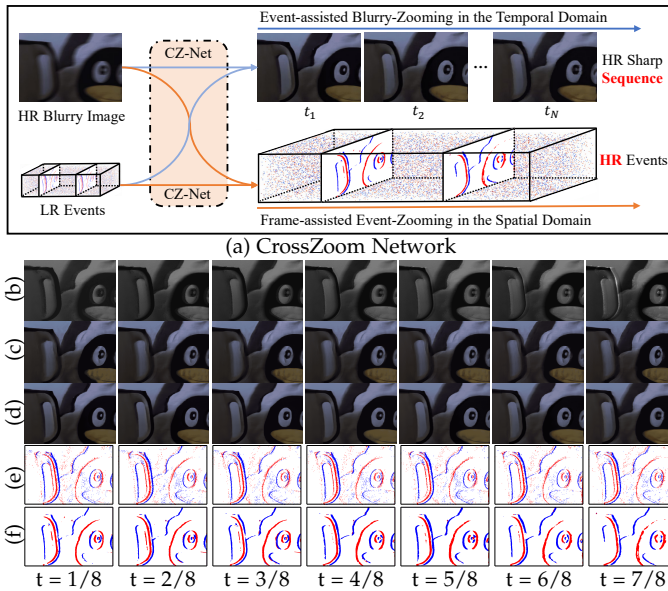


Fig. 1: Illustration of our proposed CrossZoom Network (CZ-Net), which can restore a High-Resolution (HR) sharp latent sequence (d) and HR events (f) simultaneously from a single HR blurry image and corresponding Low-Resolution (LR) Events, and comparisons to the state-of-the-art methods, *e.g.*, METR [44] (c) and EZ+RED (b) by superimposing EventZoom (EZ) [7] for event super-resolving and RED [39] for motion deblurring.

distortions, leveraging the complementary advantages of blurry images and LR events, and achieving effective MD and ESR cohesively within this unified cross-task structure.

To address these challenges, we propose a novel unified paradigm named the CrossZoom Network (CZ-Net) to achieve mutual enhancement in both spatial and temporal domains of LR events and blurry images by leveraging the complementary merits of multi-modal inputs, as shown in Fig. 1. Specifically, the Multi-scale Blur-Event Fusion (MBEF) strategy is introduced to fully exploit the scale-variant properties at different scales, guiding the super-resolving of LR events and incorporating the intra-frame information to alleviate the motion ambiguity in HR blurry image. To further harness the inherent complementarity between HR blurry images and LR events, we devise a Cross-Interaction Prediction (CIP) architecture to elevate HR intermediate features of MD and ESR branches by leveraging their respective spatiotemporal characteristics. Additionally, a blur-aware Attention-based Adaptive Enhancement (AAE) method is employed to effectively mitigate the coupled distortions and noise present in LR events and HR blurry images.

Overall, the contributions of this paper are three-fold:

- We propose a unified architecture, *i.e.*, CZ-Net, to solve MD and ESR simultaneously. To the best of our knowledge, it is the first attempt to realize the sharp image sequence reconstruction and HR event stream generation by fusing a single HR blurry image and concurrent LR events.
- We propose a cross-modality fusion module, *i.e.*, MBEF,

to achieve cross-enhancement by leveraging the scale-variant properties and effectively fusing cross-modality information. Meanwhile, blur-aware AAE and CIP modules are also presented to alleviate the distortions embedded in the LR events and reinforce the final results through the prior blur-event complementary information.

- We build a new Cross-Resolution Deblurring and Resolving (CRDR) dataset composed of paired HR sharp-blurry images and HR-LR event streams under various indoor and outdoor scenes. Extensive qualitative and quantitative comparisons demonstrate the effectiveness and robustness of our proposed CZ-Net. Codes and datasets are released at <https://besttrivencz.github.io/CZ-Net/> to facilitate future research.

2 RELATED WORK

2.1 Frame-based Motion Deblurring

The frame-based Motion Deblurring (MD) task aims to recover latent sharp images from blurry input, which is ill-posed due to the missing intra-frame motions and textures. Traditional deblurring methods often formulate the task as an inverse problem, which models a blurry image as the result of convolution with the blur kernels and can be roughly divided into blind [8], [23] and non-blind [4], [30], [30], [33], [40] architectures. Some early non-blind approaches adopt classical image deconvolution algorithms such as Wiener deconvolution, Lucy-Richardson with or without Tikhonov regularization, to restore sharp images [30], [33], [40]. On the other hand, blind image deblurring methods [2], [3], [6] aim to recover both the sharp image and the blur kernel simultaneously. In addition, various priors, including Total Variation (TV) [2], outlier image signals [6], and local maximum gradient [3] are designed to relieve the burden of ill-posedness. Generalization properties and computational efficiency usually limit the performance of these methods.

Recently, deep neural network approaches have directly learned to map blurry images to sharp latent restorations from paired datasets, achieving dominant performance [1], [5], [11], [18], [24], [42]. Techniques, including coarse-to-fine strategies [5], [24] and the imposing artificial [1] or data-driven [18] priors, have been investigated to improve the performance of latent sharp image reconstruction. To optimally balance spatial details and high-level contextualized information, MPR-Net [42] designs a multistage architecture that progressively learns restoration functions. Despite these advances, all methods mentioned above format the data-driven or optimize-based frameworks on the blurry inputs with the missing intra-frame motion and texture, leading to marginal performance and limited model generalization.

2.2 Event-based Image Deblurring

Event sensors are used for image deblurring due to their high temporal resolution [25], [26]. The first work on Event-based Motion Deblurring (EMD) [26] establishes the relationships between blurry images, events, and latent frames using an Event-Based Double Integral (EDI) model, which often suffers from heavily accumulated noise, leading to

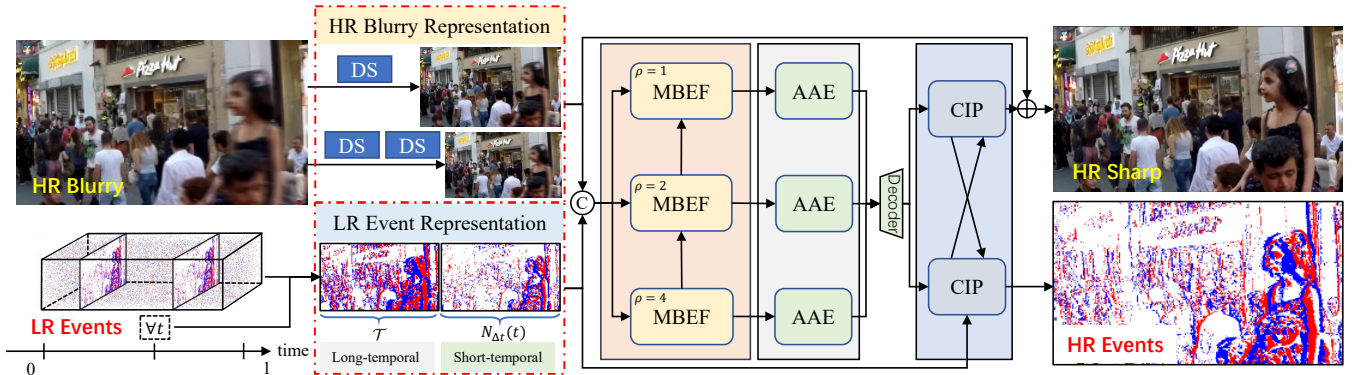


Fig. 2: Architecture of the proposed CZ-Net, which is composed of a Multi-scale Blur-Event Fusion (MBEF) module, an Attention-based Adaptive Enhancement (AAE) module, and a Cross-Interaction Prediction (CIP) module.

inaccurate details. To mitigate defects in [26], the multiple EDI (mEDI) is proposed to get a less noisy estimation from multiple images and events [25]. Learning-based approaches for EMD significantly reduce the disturbance of event noise [32], [39], [43]. Specifically, U-Net based on dual encoders is designed in [13] to perform image deblurring followed by high frame rate video generation. To alleviate performance degradation caused by data inconsistency, Xu *et al.* [39] design a semi-supervised framework using real-world events. Recently, the two-stage image restoration network EF-Net [32] combines a cross-modal attention module and symmetric cumulative event representation to fuse event and image effectively. However, the aforementioned methods only focus on restoring sharp latent images from motion-blurred images with the same spatial resolution as the events. They cannot deal with scenarios when events and blurry images have different scales.

2.3 Event Super-Resolving

The event stream acquired by detecting intensity changes is essentially a kind of spatio-temporal data. Accurate and high spatiotemporal distribution needs to be estimated for LR Event Super-Resolving (ESR). A few works [7], [20], [37], [38] are developed to achieve ESR. A multi-stage scheme is proposed in [20], sampling the events of each pixel by simulating a Poisson point process according to the specified event number and modeling a spatiotemporal filter to generate the temporal rate function. The beneficial information in HR image signals is used to guide the process of the events upsampling in an optimization framework termed GEF [37], whereas the performance of GEF is intricately linked to both the sharpness of the image and the accuracy of optical flow prediction. Duan *et al.* [7] develop a multi-task framework in denoising and super-resolving neuro-morphic events, realizing the denoising and the upsampling mapping in a noise-to-noise manner. More recently, Weng *et al.* [38] propose a recurrent neural network for reliably aggregating the spatio-temporal clues of event stream and a temporal propagation for incorporating neighboring and long-range event-aware contexts. However, they restore the HR event streams with limited temporal resolution and insufficiently accurate polarity owing to the fixed channel of the representations of the events.

3 METHOD

3.1 Problem Formulation

We first revisit the fundamental models for Motion Deblurring (MD) and Event Super-Resolving (ESR), then formulate the task of the unified Event-based motion Deblurring and Super-Resolving (uEDSR), for which we propose the Cross-Zoom Network (CZ-Net) in the subsequent subsection.

Motion Deblurring. The blurry image \mathbf{B} can be formulated as the average of the latent sharp images \mathbf{I} within the exposure interval \mathcal{T} , *i.e.*, $\kappa : \mathcal{I} \times \mathcal{T} \rightarrow \mathcal{I}$ with \mathcal{I} denoting the image subspace, leading to a significant loss in temporal resolution.

$$\mathbf{B} = \kappa(\mathbf{I}) \triangleq \frac{1}{T} \int_{t \in \mathcal{T}} \mathbf{I}(t) dt, \quad (1)$$

with T representing the duration of \mathcal{T} . Motion Deblurring (MD) aims at zooming in the temporal domain, *i.e.*, recovering sharp latent images $\{\mathbf{I}(t)\}_{t \in \mathcal{T}}$ from the blurred image \mathbf{B} ,

$$\{\mathbf{I}(t)\}_{t \in \mathcal{T}} = \text{Deblur}(t; \mathbf{B}, \mathcal{E}_{\mathcal{T}}), \quad (2)$$

where $\text{Deblur} : \mathcal{I} \rightarrow \mathcal{I} \times \mathcal{T}$ denotes an MD operator conditioned upon the auxiliary event streams $\mathcal{E}_{\mathcal{T}} \triangleq \{(\mathbf{x}_i, t_i, p_i)\}_{t_i \in \mathcal{T}}$, with \mathbf{x}_i the pixel location, t_i the time of the i -th event occurs, and $p_i \in \{-1, +1\}$ the polarity, representing brightness change directions [10]. Note that existing approaches [39], [43] are only feasible when events $\mathcal{E}_{\mathcal{T}}$ share the same scale as the blurry image \mathbf{B} .

Event Super-Resolving. Ideally, the degradation of events from High-Resolution (HR) to Low-Resolution (LR) can be represented as a spatial downsampling procedure,

$$\mathcal{E}_{\mathcal{T}}^{\rho} = \eta(\mathcal{E}_{\mathcal{T}}, \rho) \triangleq \{(\mathbf{x}_i, t_i, p_i) | (\mathbf{x}_i/\rho, t_i, p_i) \in \mathcal{E}_{\mathcal{T}}\}, \quad (3)$$

with $\rho \in \{1, 2, 3, \dots\}$ denoting the rescale factor and η indicating downsampling operator. Addressing the issue of ESR entails the prediction of the HR event stream $\mathcal{E}_{\mathcal{T}}$ from its LR counterpart $\mathcal{E}_{\mathcal{T}}^{\rho}$, which accomplishes zooming in the spatial domain for LR events, *i.e.*,

$$\mathcal{E}_{\mathcal{T}} = \text{SuperR}(\mathcal{E}_{\mathcal{T}}^{\rho}, \mathbf{I}), \quad (4)$$

where $\text{SuperR}(\cdot)$ indicates an ESR operator with the inclusion of sharp frames \mathbf{I} as the auxiliary information. However, existing frame-assisted ESR approaches degrade severely when \mathbf{I} deteriorates in the temporal domain

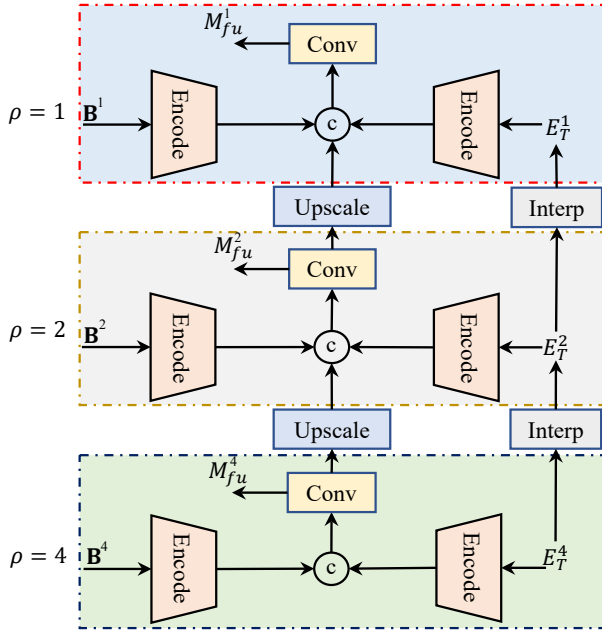


Fig. 3: Details of Multi-scale Blur-Event Fusion (MBEF) module, which integrates the blurry images and the event feature at multi-scales.

as Eq. (2) due to the vanishing of HR sharp details [37]. Moreover, limited temporal resolution and insufficiently accurate polarity of super-resolved events still prevent the applicability of existing ESR methods [7], [38].

Unified Task. The unified task is to accomplish both MD and ESR simultaneously, *i.e.*,

$$\{\mathbf{I}(t)\}_{t \in \mathcal{T}}, \mathcal{E}_{\mathcal{T}} = \text{uEDSR}(t; \mathbf{B}, \mathcal{E}_{\mathcal{T}}^{\rho}), \quad \forall t \in \mathcal{T}. \quad (5)$$

where uEDSR denotes the *unified Event-based motion Deblurring and Super-Resolving* (uEDSR) operator. Note that replacing \mathbf{B} by \mathbf{I} will degenerate uEDSR into the single ESR task as Eq. (4) and $\rho = 1$ corresponds to the single MD task as Eq. (2). However, the coexistence of degenerations for the image in the temporal domain and events in the spatial domain makes uEDSR more challenging than MD or ESR. Although it is feasible to accomplish uEDSR through a two-stage process by cascading ESR and MD without the aid of cross modalities, it often leads to suboptimal performance due to error propagation, as shown in Fig. 1 (b).

3.2 CrossZoom Network

We propose a novel CrossZoom Network (CZ-Net) to accomplish uEDSR by exploring the mutual compensations from the degraded cross-modalities, *i.e.*, the blurry image \mathbf{B} and the LR events $\mathcal{E}_{\mathcal{T}}^{\rho}$. Fig. 2 illustrates the framework of the proposed CZ-Net, which is a deep network consisting of a Multi-scale Blur-Event Fusion (MBEF) module, an Attention-based Adaptive Enhancement (AAE) module, and a Cross-Interaction Prediction (CIP) module.

3.2.1 Spatiotemporal Representation

To fully exploit the respective advantages of HR images \mathbf{B} in the spatial domain and LR event streams $\mathcal{E}_{\mathcal{T}}^{\rho}$ in the temporal domain, we sample both \mathbf{B} and $\mathcal{E}_{\mathcal{T}}^{\rho}$ at multiple scales.

Blurry Image Representation. Due to the scale-variant representation, where blurred edges become sharper after scaling down [11], we extract multi-scale sharpness information inherent in the blurry inputs \mathbf{B}^1 by DownSampling (DS) them to \mathbf{B}^2 and \mathbf{B}^4 with smaller scales. Here, the subscript numbers, 2 and 4, represent the scale reduction factors, as shown in Fig. 2.

Event Representation. We encode LR event streams $\mathcal{E}_{\mathcal{T}}^{\rho}$ into time-dependent representation frames $E_{\Delta t}^{\rho}(t)$ and entire-time event representation frames $E_{\mathcal{T}}^{\rho}$, denoted as:

$$\begin{aligned} E_{\Delta t}^{\rho}(t) &= \text{ER}(\mathcal{E}_{\mathcal{N}_{\Delta t}(t)}^{\rho}) \\ E_{\mathcal{T}}^{\rho} &= \text{ER}(\mathcal{E}_{\mathcal{T}}^{\rho}), \end{aligned} \quad (6)$$

where $\text{ER}(\cdot)$ denotes the Event Representation operator, while $\mathcal{N}_{\Delta t}(t) \triangleq \{t' \mid |t - t'| \leq \frac{\Delta t}{2}, \forall t' \in \mathcal{T}\}$ defines the interval centered around the timestamps t . The time-dependent representation, $E_{\Delta t}^{\rho}(t)$, implicitly encodes timestamp information, which is crucial to guide the recovery of sharpness at specific given timestamps t . On the contrary, the whole-time representation, $E_{\mathcal{T}}^{\rho}$ incorporates comprehensive motion information spanning the entire exposure time interval \mathcal{T} and effectively mitigates motion ambiguity in the MD task. The final event representation frame E^{ρ} is obtained by concatenating the $E_{\Delta t}^{\rho}(t)$ and $E_{\mathcal{T}}^{\rho}$, and we employ the Voxel Grid method [46] as ER to quantize information into eight bins.

3.2.2 Multi-scale Blur-Event Fusion

Another challenge for CZ-Net is the effective utilization of complementarities between degraded inputs \mathbf{B} (suffering from temporal collapse) and $\mathcal{E}_{\mathcal{T}}^{\rho}$ (undergoing spatial collapse) which have a different spatial resolution. Hence, the MBEF module is designed to perform cross-enhancement by fusing B^R , which holds spatial multi-scale sharpness information, with E^R , containing temporal multi-scale intra-frame motion across various scales. Here, $R \triangleq \{1, 2, 4\}$ represents the set of scale reduction factors.

Specifically, as depicted in Fig. 3, we initiate the process by obtaining E^R at various scales by applying two bilinear interpolation operators. Subsequently, we extract multi-scale blurry and event features, denoted as M_b^R and M_e^R , respectively, by utilizing dedicated blur- and event-encoding networks. Then we derive the blur-event fusion feature M_{fu}^4 along with its associated upscaled feature $U^{2 \times}$, denoted as:

$$\begin{aligned} M_{fu}^4 &= \text{Conv}(M_b^4 \oplus M_e^4) \\ U^2 &= o(\text{Upscale}(M_{fu}^4)), \end{aligned} \quad (7)$$

where the symbol \oplus denotes the concatenation operation; the operator $\text{Conv}(\cdot)$ corresponds to double dilated Convolutional layers followed by the activation function Relu; the $\text{Upscale}(\cdot)$ means the use of a transposed layer for feature upscaling with trainable parameters; and the mapping function $o(\cdot)$ is required for generating an intermediate upscaled feature map, which is achieved through a single convolutional layer. We extend this procedure to encompass blur-event fusion features M_{fu}^2 with scale reduction factor of 2, with the omitting of 1 for simplicity, which can be formulated as

$$\begin{aligned} M_{fu}^2 &= \text{Conv}(M_b^2 \oplus M_e^2 \oplus U^2) \\ U^1 &= o(\text{Upscale}(M_{fu}^2)). \end{aligned} \quad (8)$$

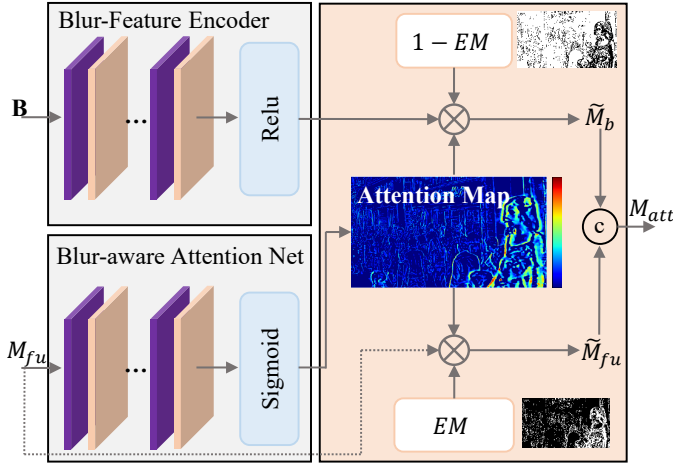


Fig. 4: Architecture of the Attention-based Adaptive Enhancement (AAE) module, equipped with a blur-aware attention and Event Mask (EM) to alleviate the coupled distortions embedded in HR blurry image and LR events.

The concatenation terms incorporate information from the previous scale U^2 , enhancing the fusion feature M_{fu}^2 . By employing the MBEF module, we acquire fusion features M_{fu}^R that effectively leverage the complementarities between \mathbf{B} and $\mathcal{E}_{\mathcal{T}}^p$, facilitating simultaneous cross-zooming in the temporal domain for blurry image \mathbf{B} and in the spatial domain for LR events $\mathcal{E}_{\mathcal{T}}^p$.

3.2.3 Attention-based Adaptive Enhancement

The fusion-based features M_{fu} estimated by the MBEF operator still suffer from the imperfections of LR events for two primary reasons: i) Values in M_{fu} that correspond to the sparse regions in LR events are inferred from surrounding isolated values, achieved by incrementally expanding receptive fields; ii) Portions of representations within M_{fu} originate from noise inherent in LR events. Both situations result in low-confidence, unreliable features, which pose challenges for subsequent tasks such as MD and ESR. To this end, we introduce the Attention-based Adaptive Enhancement (AAE) module, designed to incorporate the M_{fu} and \mathbf{B} adaptively by using a blur-aware attention map and an event mask. This process assigns less attention to invalid representations in M_{fu} while enhancing the confidence of the features derived from \mathbf{B} that provide valuable clues, including multi-scale sharpness information. As illustrated in Fig. 4, the proposed AAE module consists of two main steps: Blur-Aware Attention Generation and Adaptive Fusion. These steps take M_{fu} and the blurry image \mathbf{B} as inputs and produce an adaptive attention-based feature denoted as M_{att} . For brevity, we omit superscripts that indicate different scale factors.

Blur-Aware Attention Generation. Blur-aware attention map is used as a gating function to deliver more weight to blurry pixels that equal the magnitude of motion. Let M_{fu} be an input tensor, BA-Net a Blur-aware Attention Network that learns the map from M_{fu} to a significant vector $Y = \text{BA-Net}(M_{fu})$, consisting of a double Conv operator in Eq. (7). An attention map A can be computed

by

$$A = \sigma(Y) = \text{Sigmoid}(\text{BA-Net}(M_{fu})). \quad (9)$$

Akin to [27], we take the difference between the blurry and sharp frames at timestamps t and subsequently apply thresholding to generate the ground-truth blur mask. Furthermore, instead of applying the softmax, which is the sum-to-one constraint, we use a sigmoid activation function which only constrains attention importance values ranging from 0 to 1: $A = 1/(1 + \exp(-Y))$. Then, we supervise the BA-Net by the pixel-wise l_1 norm loss as

$$\mathcal{L}_{att} = \|\hat{A} - A\|_1, \quad (10)$$

where \hat{A} is the difference map between latent sharp and blurry images. Consequently, the attention map A contains blurry information that denotes the confidence of the events emitted.

Adaptive Enhancement. The blur-aware attention map A , in conjunction with the binary Event Mask denoted as EM that signifies the occurrence or absence of emitted events, is employed to assign lower attention values to areas with no motion blur yet events activated for suppressing the invalid feature in M_{fu} caused by the imperfection of noise and sparsity. Mathematically, we can calculate the enhanced attention-based feature \tilde{M}_{fu} as

$$\tilde{M}_{fu} = [W_1 \otimes M_{fu_1}, W_1 \otimes M_{fu_2}, \dots, W_1 \otimes M_{fu_m}], \quad (11)$$

where $W_1 = A \otimes EM$ denotes the weighting map calculated from blur-aware attention map A and event mask EM with a value of 1 assigned to event pixels and 0.1 to non-event-pixels, \otimes is an element-wise multiplication, and suffix m represents the channel number of M_{fu} . Furthermore, for areas in M_{fu} where events are absent, but motion blurs exist, the feature \tilde{M}_b obtained by a blur-feature encoder, consisting of a double Conv operator in Eq. (7), contains multi-scale sharpness information and is given more attention to enhancing the deblurring results. The enhanced feature \tilde{M}_b can be represented as

$$\tilde{M}_b = [W_2 \otimes M_{b_1}, W_2 \otimes M_{b_2}, \dots, W_2 \otimes M_{b_n}], \quad (12)$$

where $W_2 = A \otimes (1 - EM)$ and the suffix n means the channel number of M_b . The final adaptive fusion feature M_{att} from the blurry image and events can be obtained by concatenating the \tilde{M}_b and \tilde{M}_{fu} . The calculation of the adaptive fusion feature M_{att} is applied to every branch with three resolutions. After obtaining adaptive fusion features M_{att}^R , a Multi-Scale Decoder (MSD) module is applied for feature decoding and enhancement and generates the decoded features $\{M_{md}^1, M_{esr}^1\} = \text{Conv}(M_{att}^1 \oplus M_{att}^{2\uparrow} \oplus M_{att}^{4\uparrow\uparrow})$ for MD and ESR, which $(\cdot)^\uparrow$ denotes the combination of upscaling and convolutional layers, as shown in Fig. 2.

3.2.4 Cross-Interaction Prediction

The Cross-Interaction Prediction (CIP) module is designed to further enhance the intermediate feature map by integrating cross-task representations, and the details of CIP are shown in Fig. 2. Specifically, the predicted sharp images can be computed by

$$\mathbf{I}^1 = o(\text{Conv}(M_{md}^1) \oplus \text{Conv}(M_{esr}^1)) + \mathbf{B}^1, \quad (13)$$

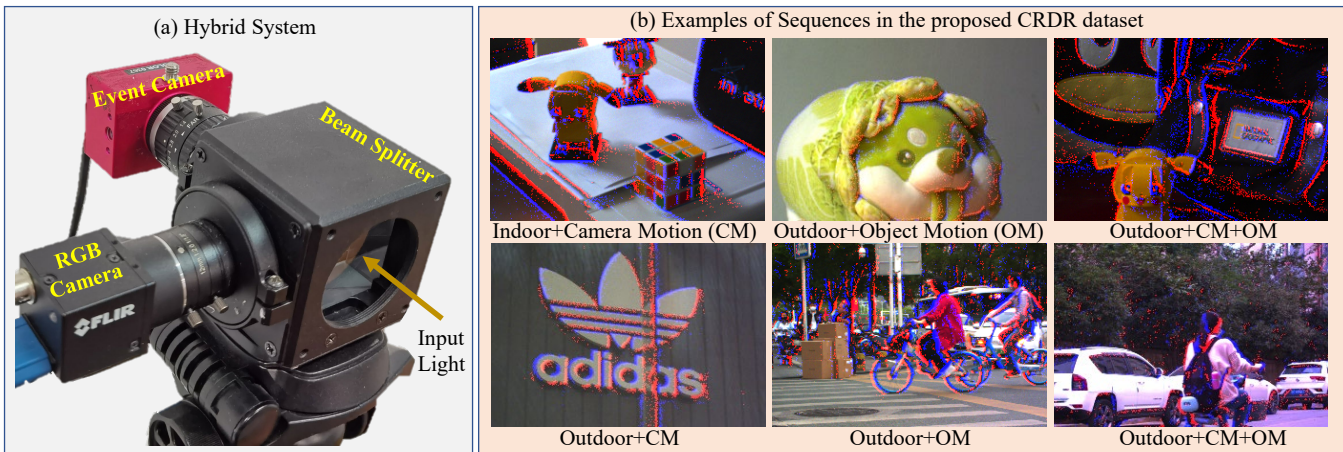


Fig. 5: (a) The illustration of a beam splitter-based hybrid system for building the CRDR. (b) Sequence samples of the proposed CRDR dataset.

TABLE 1: Details about the proposed CRDR dataset. In total, the dataset consists of 76 sequences for both indoor and outdoor scenarios.

Split	Scenes	#Seq	#Events (M)	#Pairs
Train	Buildings	4	23.43	299
	Downstairs	2	18.76	157
	Campus	18	93.46	1153
	Pedestrians	11	31.42	528
	Streets	15	59.33	978
	Indoor	5	35.16	387
		55	261.56	3502
Test	Buildings	2	8.54	113
	Downstairs	1	6.52	39
	Campus	7	33.71	330
	Pedestrians	3	22.77	138
	Streets	5	38.51	205
	Indoor	3	5.97	57
		21	116.02	882
Total		76	377.58	4384

where we add the original blurry image to generate the final predicted sharp image \mathbf{I}^1 . For final HR event prediction, the formula can be defined as

$$\tilde{E}^1(t) = o(\text{Conv}(M_{esr}^1) \oplus \text{Conv}(M_{md}^1) \oplus E_{\Delta t}^1(t)), \quad (14)$$

which concatenates the time-dependent feature $E_{\Delta t}^1(t)$ to assist in generating HR events at timestamps t .

3.3 Optimization

The loss of Motion Deblurring. We supervise the estimation of latent sharp images with the ℓ_1 norm between the predicted sharp images $\mathbf{I}(t)$ and the ground truth sharp images $\hat{\mathbf{I}}(t)$, which is defined as

$$\mathcal{L}_{md} = \|\mathbf{I}(t) - \hat{\mathbf{I}}(t)\|_1. \quad (15)$$

Training CZ-Net at the referenced timestamps with the corresponding ground-truth sharp images is straightforward. When it comes to training at non-referenced timestamps, it can be challenging due to the lack of reference sharp images. As a result, a video interpolation method, *i.e.*, RIFE [14], is applied to generate reference sharp images at non-referenced timestamps, enabling the supervision of the latent restoration of those non-referenced timestamps.

The loss of Event Super-Resolving. Similarly, the event super-resolving task is also supervised by the ℓ_1 norm between the predicted HR event \tilde{E}_t^1 and the ground truth HR event \hat{E}_t^1 , which can be defined as

$$\mathcal{L}_{esr} = \|\tilde{E}_t^1(t) - \hat{E}_t^1(t)\|_1. \quad (16)$$

Thus, the overall loss function for CZ-Net is defined as

$$\mathcal{L}_{total} = \mathcal{L}_{md} + \alpha\mathcal{L}_{esr} + \beta\mathcal{L}_{att}, \quad (17)$$

where α, β are the balancing parameters.

4 CRDR DATASET

To our knowledge, no publicly released dataset is available yet for uEDSR task with Low-Resolution (LR) events. It motivates us to build a new dataset for Cross-Resolution Deblurring and Resolving (CRDR) containing paired HR *sharp-blurry* images and the corresponding HR-LR event streams.

System Setup. To simultaneously collect images and events, we build a hybrid camera system composed of an LR DAVIS346 event camera of resolution 346×260 and an HR FLIR BlackFly U332S4 RGB camera of resolution 2048×1536 working at a frame rate of 118 FPS, as shown in Fig. 5 (a). A beam splitter connects two cameras to achieve minimum spatial parallax between RGB frames and events. Since two cameras provide vision perceptions of different modalities and spatial resolutions, calibrations in both spatial and temporal domains are essential to ensure alignments between collected RGB frames and events.

Spatial and Temporal Calibration. The spatial and temporal calibration ensures that LR events and HR RGB images are time synchronized and share the same field of view. We employ the Active Pixel Sensor (APS) frames output from the DAVIS346 event camera to achieve spatial calibration since APS frames and events share the same light path and spatial resolution. The homography between two cameras can be estimated to achieve the geometric calibration, where the LR APS frames and HR RGB images are matched using SIFT [22] and RANSAC [9]. Regarding temporal synchronization, we only have to estimate the time offsets between two cameras by searching the timestamps with the highest

TABLE 2: Quantitative comparisons of the proposed CZ-Net to the state-of-the-art motion deblurring methods on GoPro and CRDR datasets. The best performance is in **bold** and the second best is underlined. The symbol / denotes infeasible to reconstruct sharp sequences.

Methods	Color	Single frame restoration				7 frames restoration			
		GoPro		CRDR		GoPro		CRDR	
		PSNR \uparrow	SSIM \uparrow	PSNR \uparrow	SSIM \uparrow	PSNR \uparrow	SSIM \uparrow	PSNR \uparrow	SSIM \uparrow
DeblurGanV2 [19]	✓	30.98	0.9176	23.66	0.6973	/	/	/	/
MPRNet [42]	✓	32.66	0.9590	24.36	0.7553	/	/	/	/
MotionETR [44]	✓	29.72	0.9305	21.46	0.6818	23.37	0.7328	20.21	0.6400
BL+EF-Net [32]	✓	24.38	0.7963	22.84	0.7083	/	/	/	/
EZ [7]+EF-Net [32]	✓	26.58	0.8440	22.83	0.7181	/	/	/	/
BL+E-CIR [31]	✗	21.39	0.7907	14.34	0.5024	21.28	0.7852	14.21	0.4988
EZ [7]+E-CIR [31]	✗	20.31	0.7231	13.40	0.4535	20.11	0.7146	13.31	0.4406
eSL-Net $_{4\times}$ [34]	✗	22.29	0.6790	14.32	0.5318	21.69	0.6631	13.41	0.4811
RED [39]+DASR [35]	✗	22.26	0.7210	13.45	0.4761	21.24	0.6720	13.36	0.4741
BL+eSL-Net [34]	✗	22.19	0.7255	13.86	0.4784	20.38	0.6946	13.22	0.4591
BL+RED [39]	✗	25.79	0.8514	18.75	0.6494	24.18	0.8190	16.49	0.6276
EZ [7]+eSL-Net [34]	✗	20.52	0.6673	14.35	0.5281	21.64	0.7109	14.18	0.5201
EZ [7]+RED [39]	✗	25.51	0.8209	22.89	0.6954	22.60	0.7582	19.55	0.6203
CZ-Net-G	✗	35.00	0.9659	<u>26.28</u>	<u>0.7407</u>	<u>31.61</u>	<u>0.9302</u>	<u>25.01</u>	<u>0.7274</u>
CZ-Net-C	✓	<u>34.74</u>	<u>0.9642</u>	26.93	0.7835	31.78	0.9322	25.52	0.7693

values of structural similarity [36] between stacked LR event frames and the gradient maps of downsampled HR RGB frames. Fig. 6 illustrates a typical example of the calibration results.



(a) Misaligned Scenes

(b) After Global Alignment

Fig. 6: Alignment of standard frames with events. Aggregated events (red is positive, and blue is negative) are overlain with the standard frame.

Data Collecting. As shown in Tab. 1, we collect a total of 76 sequences comprised of both image sequences and event streams with diversity in terms of scenes, *i.e.*, indoor and outdoor, and motion types, *i.e.*, camera and object motion. Some representative examples are visualized in Fig. 5 (b). The sharp HR images are captured with slow and stable camera movement to avoid motion blur. Furthermore, to preserve maximum effectiveness information after spatial and temporal calibration, we crop the RGB frames and events to 768×1152 and 192×288 , respectively, by taking the center of them as the basement. Motion blurs are synthesized by averaging adjacent 7 HR sharp frames, resulting in 4384 pairs with blurred and sharp images, and the HR-Event streams are synthesized using the event simulator [28]. We randomly select 55 sequences as the training set and the rest as the testing set. The data-splitting details of our CRDR dataset are summarized in Tab. 1.

5 EXPERIMENTS AND ANALYSIS

In this section, the performance of our CZ-Net is evaluated on both MD and ESR tasks. We first present the experimental settings in Sec. 5.1, including details on datasets and implementations. Afterward, quantitative and qualitative comparisons of our CZ-Net are made to the state-of-the-art MD methods on restorations of a single latent sharp image in Sec. 5.2.1 and a continuous-time video sequence in Sec. 5.2.2. We further evaluate the performance of CZ-Net on the ESR task in Sec. 5.3. Ablations on the effectiveness of network architecture and loss functions are finally presented in Sec. 5.4.

5.1 Experimental Settings

Datasets. Two datasets are employed for network training and evaluation, *i.e.*, the synthetic dataset simulated over GoPro [24] and the real-world CRDR dataset built in this paper. Both datasets contain paired *HR-LR* events and *HR sharp-blurry* images. We have presented the details of our CRDR dataset in Sec. 4. Regarding the synthetic dataset, we build it upon the GoPro dataset [24], which is widely adopted to evaluate the MD performance [42], [44] and recently used to benchmark the Event-based MD (EMD) task [26], [39], [43]. Specifically, we first downsample the HR sharp images from the GoPro dataset and then simulate the LR events by an open-sourced event simulator, *i.e.*, ESIM [28], from the downsampled LR images. At the same time, we synthesize the HR blurry images by averaging the adjacent HR sharp images. The splitting of the training and testing for the synthetic dataset is identical to the official open-sourced GoPro dataset.

Training Details and Evaluation Metrics. The proposed CZ-Net is implemented by PyTorch and trained on an NVIDIA GeForce RTX 3090 for 200 epochs with 4 batch sizes by default. Furthermore, we augment the training data by flipping (horizontal, vertical, and horizontal-vertical) and rotating (random angles ranging from -10° to 10°) to

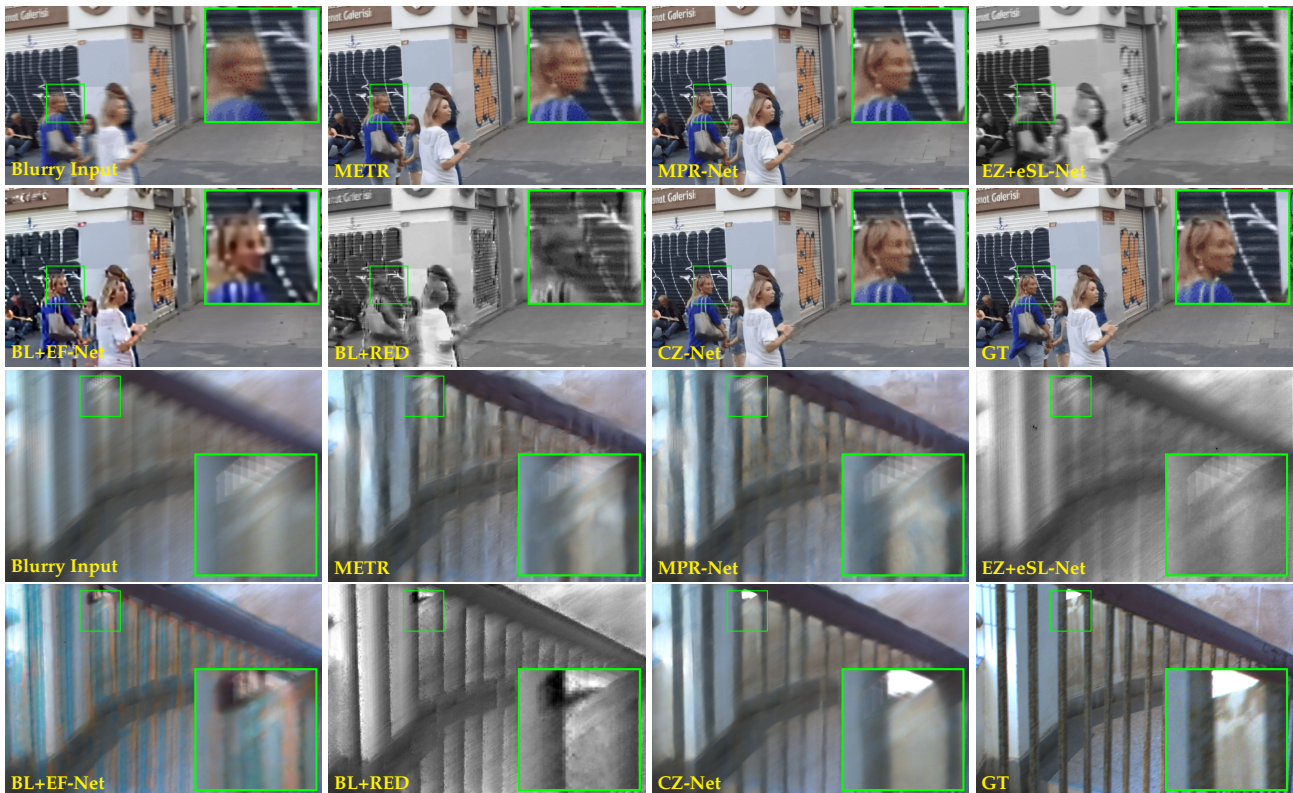


Fig. 7: Qualitative comparisons of different deblurring methods on the GoPro (top two rows) and CRDR (bottom two rows) datasets. The magnified parts are displayed for clarity. From left-top to right-bottom are, respectively, blurry images and deblurring results by METR [44], MPRNet [42], EventZoom (EZ) [7]+eSL-Net [34], BL+EF-Net [32], BL+RED [39], the proposed CZ-Net, and Ground Truth.

enhance the robustness of our CZ-Net. We use the ADAM optimizer [17] with an initial learning rate of 10^{-4} , and the exponential term decays by 0.98 for every 5 epoch. The weighting factors α and β in Eq. (17) are set to 1 and the Δt in Eq. (6) is set to 0.2. We use Structural Similarity (SSIM) [36] and Peak Signal to Noise Ratio (PSNR) as performance metrics for the MD and ESR tasks following [7], [38], [39].

5.2 Performance of Motion Deblurring

We first evaluate our CZ-Net for the MD task. Qualitative and quantitative comparisons are made to state-of-the-art (SOTA) frame-based MD methods, including Deblur-GanV2 [19], METR [44], and MPRNet [42], and Event-based MD (EMD) methods, including RED [39], eSL-Net [34], E-CIR [31], and EF-Net [32]. We use their official code and test with the default parameter settings. Different from our CZ-Net, existing EMD approaches are implemented by superimposing an individual super-resolution module to bridge the scale gap between LR events and HR images, either in the event domain by BiLinear upsampling (BL) and EventZoom (EZ) [7] or in the image domain by DASR [35]. Specifically, we denote BL/EZ+eSL-Net/RED/EF-Net/E-CIR as ESR-then-EMD approaches and RED+DASR as EMD-then-ESR approaches. Note that eSL-Net [34] itself can super-resolve the LR blurry image. Thus, we implement it by first downsampling the HR blurry image and then super-

resolving the downsampled LR blurry image with the LR events, denoted as eSL-Net $_{4\times}$.

5.2.1 Results of Single Frame Restoration

Quantitative results. The quantitative results of the single-frame prediction on the GoPro and the proposed CRDR dataset are shown in Tab. 2. Our CZ-Net outperforms state-of-the-art methods by a large margin. Specifically, CZ-Net achieves 8.3/6.9 dB and 0.158/0.151 improvements in PSNR and SSIM on the GoPro and CRDR datasets. The superior performance of CZ-Net is attributed to its effective utilization of flawed LR events, which still contain essential intra-frame information on motion and texture. Among the EMD methods, our proposed CZ-Net exhibits significant improvements over the two-stage cascaded methods, *i.e.*, BL+EF-Net, BL+E-CIR, RED+DASR, BL+eSL-Net, BL+RED, EZ+EF-Net, EZ+E-CIR, EZ+eSL-Net, and EZ+RED, which validate the effectiveness of our unified framework that can eliminate the accumulated errors between the separated ESR and MD tasks.

Qualitative results. We further qualitatively evaluate the performance in the GoPro and CRDR datasets, and qualitative results for visual comparison are shown in Fig. 7. On the one hand, the results in the GoPro dataset are shown in the top two rows of Fig. 7. The results estimated by frame-based SOTA methods, *i.e.*, MPRNet [42] and METR [44], suffer artifacts and distortions, degenerating the overall quality of the deblurred image. Moreover, the two-stage architecture combining the ESR methods accumulates defects



Fig. 8: Qualitative comparisons of the sequence restoration where 15 latent frames are restored from one single blurry image on the CRDR dataset by RED-Net, METR (+ Interpolation), and our proposed CZ-Net. Only the first 11 consecutive images of the entire sequence are shown here.

in each independent task, leading to severe degeneration of the deblurring results. On the contrary, Our CZ-Net can obtain accurate reconstructions that exhibit the most similar appearances to the ground-truth sharp images. On the other hand, the bottom two rows of Fig. 7 present qualitative results on the CRDR dataset with *real-world* LR events in more challenging scenarios. The MPRNet [42] and METR [44] fail to restore sharp latent images without the aid of events due to the increased complexities of the scene in motions and textures. Frame-based methods are ineffective in recovering targets details, *e.g.*, *handrails*. Cascaded event-based methods, *i.e.*, BL+RED, cannot restore sharper contours of targets and suffer suboptimal solutions owing to the error propagation. Our CZ-Net predicts results with sharper edges and smoother surfaces than its competitors, demonstrating the effectiveness of our unifying architecture and the AAE mechanism in suppressing invalid features caused by LR events.

5.2.2 Results of Video Sequence Restoration

Video sequence recovery from a single blurry image is more challenging than single-frame reconstruction. To our knowl-

edge, most of the existing frames-based MD approaches can only predict a single frame, *i.e.*, DeblurGanV2 [18] and MPRNet [42]. Thus, we only compare our proposed CZ-Net with the methods, *i.e.*, METR, EZ+RED, EZ+eSL-Net, BL+eSL-Net, and BL+RED, that can predict latent sharp sequence from a single blurry image. Quantitative and qualitative results are given in Tab. 2 and Fig. 8, respectively.

Regarding the quantitative results, we evaluate the performance of MD methods concerning seven reconstructed latent sharp images from a single blurry input. On the GoPro dataset, our CZ-Net outperforms other methods regarding SSIM (up to 0.1722 improvement) and PSNR (up to 6.04 dB improvement). On the CRDR dataset, our CZ-Net performs best, validating its effectiveness in handling real-world events.

To explore the superiority of our CZ-Net in recovering sharp latent sequences, we compare BL+RED and METR in reconstructing 15 continuous frames of the CRDR dataset. Since RED and METR can only output 7 latent frames, we cascade these methods and the video frame interpolation method, *i.e.*, RIFT [14] to achieve continuous-time restoration, where 7 deblurred images are interpolated to 15

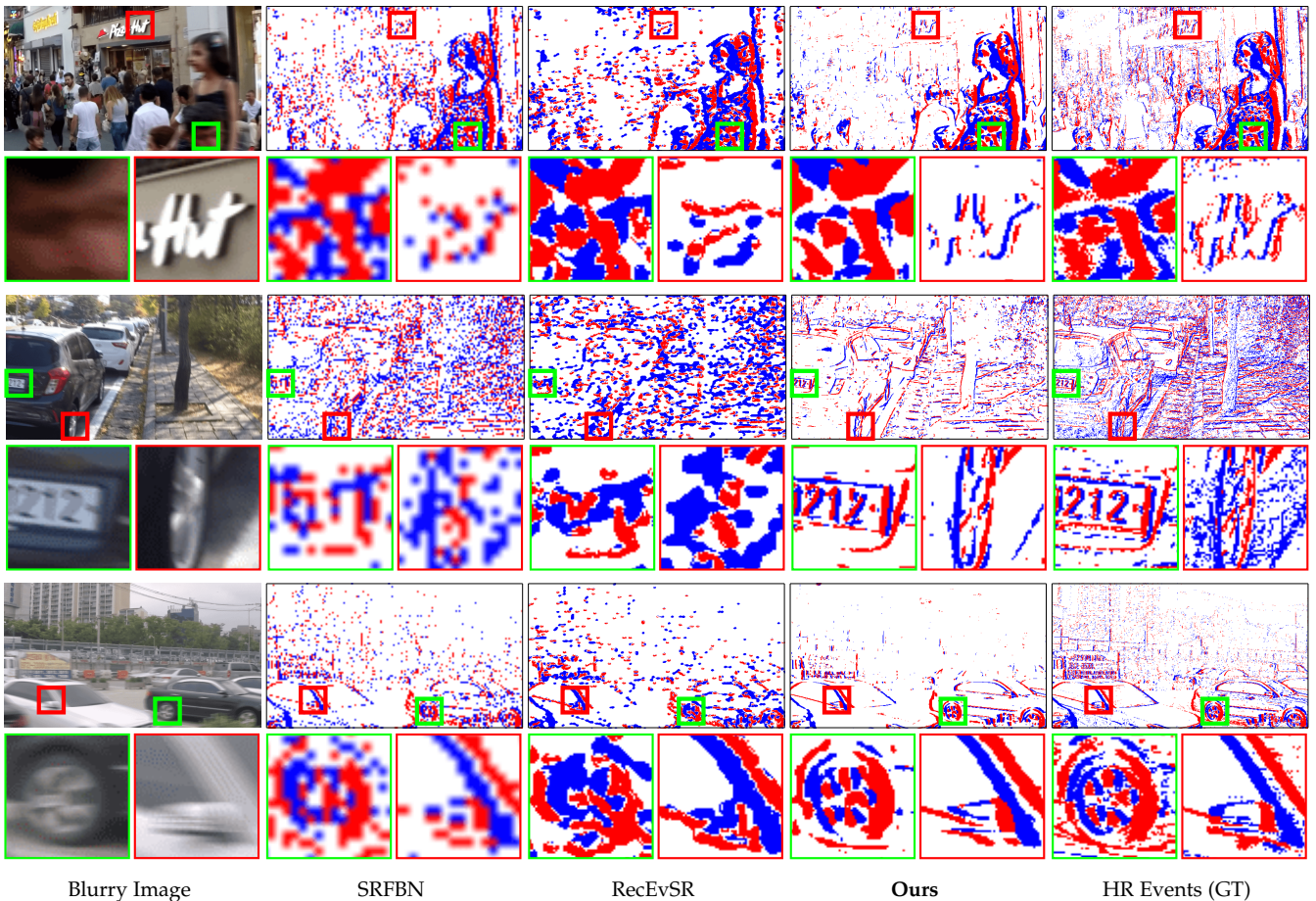


Fig. 9: Qualitative ESR results on the GoPro dataset, where our CZ-Net is compared with SRFBN and RecEvSR.

images. The qualitative results are shown in Fig. 8. METR can restore the sharp frame at the intermediate exposure time. Still, the effects in the whole temporal domain degrade severely due to the inconsistency between the motion assumption and the scenes with complex motions. Moreover, BL+RED performs with a slight improvement in both spatial and temporal domains compared to METR, thanks to the introduction of LR events. However, its details still suffer artifacts, *e.g.*, halo effects, since deblurring errors might be propagated to the interpolation stage and accumulated to the restorations of the non-referenced timestamps. Our CZ-Net predicts results with sharper edges and smoother inter-frame transitions than the SOTA methods at non-reference and reference timestamps.

5.3 Performance of Event Super-Resolving

The uEDSR is a joint task in which both MD and ESR should be addressed. Therefore, we compare our CZ-Net to the state-of-the-art frame-based SR methods, *i.e.*, SRFBN [21], and the event-based method, *i.e.*, RecEvSR [38]. Furthermore, we retrain RecEvSR [38] on the GoPro and CRDR datasets using the official code with the default parameter setting for a fair comparison.

5.3.1 Qualitative Results

We evaluate the performance qualitatively on the GoPro and CRDR datasets. The results are visualized in Fig. 9 for the

TABLE 3: Quantitative comparisons of ESR in terms of E2VID results on the GoPro dataset, where SSIM (\uparrow) is adopted as the metric. **Bold** and underlined numbers represent the best and second-best performance.

Sequence	BL	SRFBN	RecEvSR	CZ-Net
#0	0.2822	<u>0.3014</u>	0.2751	0.3638
#1	0.1910	<u>0.1945</u>	0.1693	0.1963
#2	0.3001	<u>0.3286</u>	0.2766	0.3676
#3	0.2901	<u>0.3179</u>	0.2473	0.3815
#4	0.2699	<u>0.2975</u>	0.2688	0.3421
#5	0.4277	<u>0.4422</u>	0.3398	0.4574
#6	0.3783	<u>0.4033</u>	0.2911	0.4340
#7	0.4239	0.4423	<u>0.4749</u>	0.5202
#8	0.4683	<u>0.4920</u>	0.3746	0.5009
#9	<u>0.4409</u>	0.4595	0.3119	0.4380
#10	0.2237	<u>0.2419</u>	0.2190	0.3155
Average	0.3394	<u>0.3598</u>	0.2955	0.3930

GoPro dataset and Fig. 10 for the CRDR dataset.

Fig. 9 illustrates the qualitative results on the GoPro dataset under the middle time of the exposure period of the corresponding blurry image. The results of the SRFBN and RecEvSR methods still suffer texture discontinuities and jagged distortions, thus failing to recover the *license plate* of the second example in Fig. 9. On the contrary, our CZ-Net gives precise HR event reconstructions in the spatial domain, exhibiting the most similar appearances to ground-truth HR events.

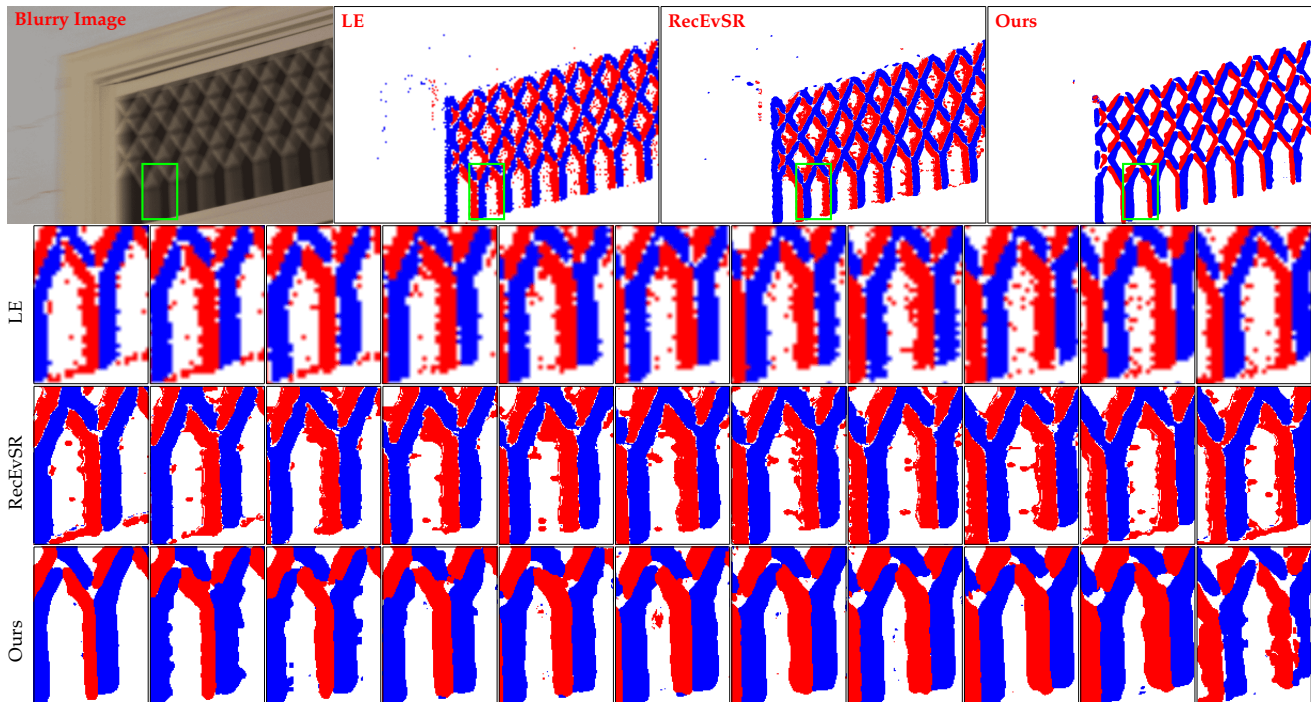


Fig. 10: Qualitative comparisons of ESR on the CRDR dataset by SRFBN, RecEvSR, and our CZ-Net.

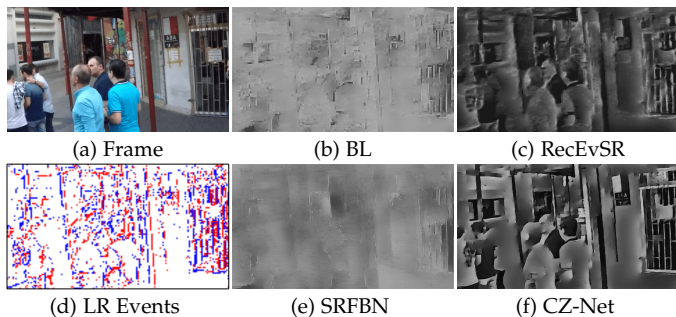


Fig. 11: Visual comparisons of video reconstruction among BiLinear (BL), SRFBN [21], RecEvSR [38] and ours CZ-Net on the GoPro dataset.

Fig. 10 visualizes the reconstruction of 11 sequences at timestamps with equal intervals to demonstrate the superiority of our CZ-Net. In addition to the advantages in terms of texture details in the spatial domain, our CZ-Net also has significant advantages in terms of temporal accuracy and noise robustness compared to RecEvSR as illustrated in the last three rows of Fig. 10.

5.3.2 Quantitative Results on Downstream Applications

We investigate the performance of BiLinear (BL) upsampling, SRFBN [21], RecEvSR [38], and our CZ-Net on video reconstruction application over the GoPro dataset. The E2VID [29] is chosen as the benchmark algorithm for event-to-video reconstruction with the evaluation metric of SSIM. The numerical results are presented in Tab. 3. Our CZ-Net outperforms others in most sequences, demonstrating its superior performance, and our results consistently exhibit the best average performance across all sequences. Moreover, the visual comparison results are displayed in

TABLE 4: Ablation study of MBEF, AAE, and CIP in our method on the CRDR dataset. **Bold** and underlined numbers represent the best and the second-best performance.

Case	MBEF	AAE	CIP	PSNR \uparrow	SSIM \uparrow
#0	✓			24.40	0.7411
#1		✓		25.39	0.7593
#2			✓	25.59	0.7622
#3	✓	✓		25.67	0.7640
#4	✓		✓	<u>26.34</u>	<u>0.7750</u>
#5		✓	✓	25.74	0.7654
#6	✓	✓	✓	26.93	0.7836

TABLE 5: Ablation study supervision on the CRDR dataset. **Bold** numbers represent the best performance.

Ex.	\mathcal{L}_{md}	\mathcal{L}_{esr}	\mathcal{L}_{att}	PSNR \uparrow	SSIM \uparrow
A	✓			25.43	0.7624
B	✓	✓		25.86	0.7653
C	✓		✓	26.05	0.7712
D	✓	✓	✓	26.93	0.7836

Fig. 11. These results demonstrate that our CZ-Net captures fine perceptual details while the comparison methods (BL, SRFBN, and RecEvSR) generate noticeable artifacts.

5.4 Ablation Study

In this subsection, we conduct a comprehensive set of ablation studies to investigate the design choices of our method. Firstly, we demonstrate the individual performance contribution of each module in the network architecture (Tab. 4 and Figs. 12 and 14). Then, we analyze the role of each supervision during the training phase (Tab. 5 and Fig. 13).

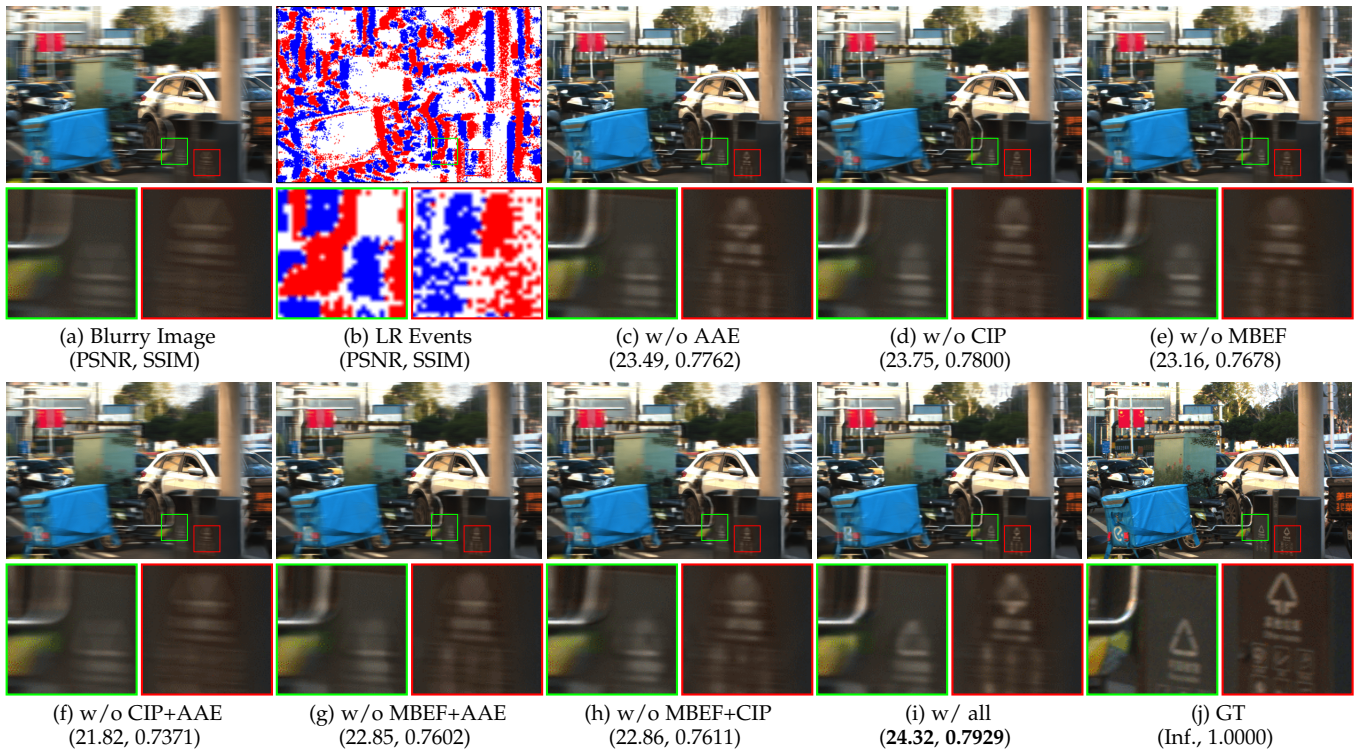


Fig. 12: Qualitative ablations of MBEF, AAE and CIP modules in CZ-Net on the CRDR dataset.

5.4.1 Network Architecture

The proposed network is composed of a Multi-scale Blur-Event Fusion (MBEF) module, an Attention-based Adaptive Enhancement (AAE) module, and a Cross-Interaction Prediction (CIP) module. Ablation studies are conducted on the CRDR dataset with real-world LR events, where seven different experiments are implemented to analyze the effectiveness of each module. Quantitative and qualitative results are shown in Tab. 4 and Fig. 12, respectively.

First, we remove the MBEF module (Case 1, 2, and 5 in Tab. 4) and replace it with a single-scale fusion module by upsampling the LR events followed by convolutional layers. Compared to it, the full CZ-Net utilizes MBEF for scale-variant enhancement by adapting parallel fusion branches at multi-scale levels. Such a fusion mechanism significantly improves PSNR (1.19 dB) and SSIM (0.0182). Qualitative results in Fig. 12 comparing (c) with (g), (d) with (h), and (i) with (e) demonstrate that CZ-Nets with the MBEF module give sharper results than networks without it, validating the effectiveness of the MBEF module.

Moreover, the AAE module is designed to alleviate the distortions caused by the low spatial resolution of the LR events. The deletion of this module (Case 0, 3, and 4) brings performance degeneration, *i.e.*, 0.59 dB and 0.0086 in terms of PSNR and SSIM, and the corresponding visualization results shown in Fig. 12 (c), (f), and (g) suffer severe artifacts. Additionally, the feature visualizations of the AAE module are depicted in Fig. 14. Owing to the tremendous coupled distortions and noise in LR events (b), the area in the event feature map (d) and sharp pixels (a) is invalid and should be suppressed. Compared with the input feature map (d), the AAE module’s output feature map (e) effectively reduces

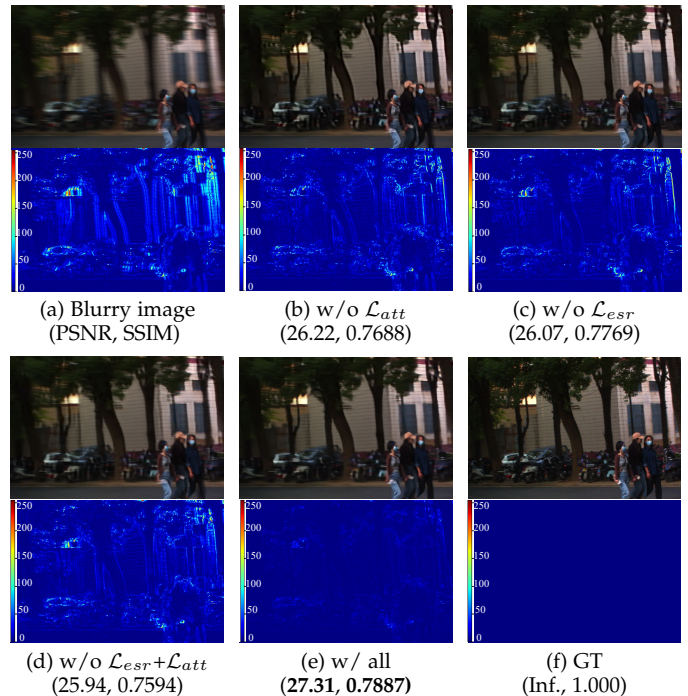


Fig. 13: Qualitative ablations of each supervision and their absolute differences to the ground-truth reference. Metric performance (*i.e.*, PSNR \uparrow /SSIM \uparrow) on estimating the latent sharp image over the CRDR dataset.

the confidence in such valid areas, validating its ability for invalid feature suppression.

Furthermore, we exclude the CIP module (cases 0, 1, and

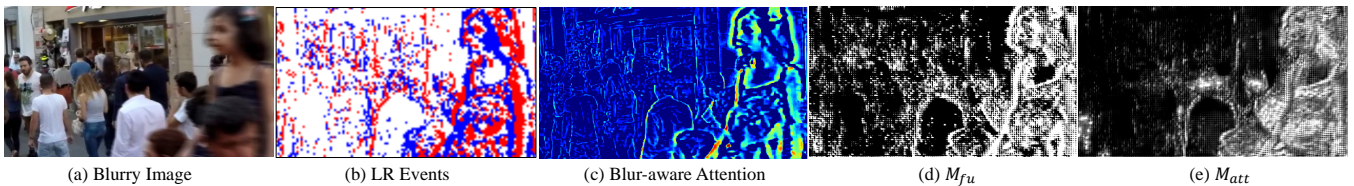


Fig. 14: Visualization of input (d) and output (e) feature maps of AAE on the GoPro dataset.

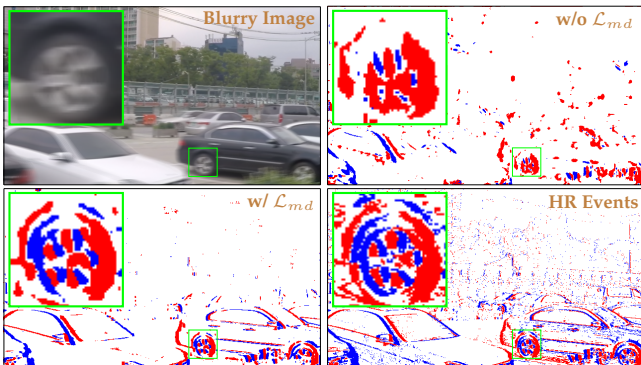


Fig. 15: Qualitative ablation of the deblurring supervision.

3 in Tab. 4) and substitute it with a pair of conventional dual-branch convolutional layers with an equivalent number of parameters. In contrast, the full CZ-Net integrates CIP for frame-event complementary enhancement by adapting a feature cross-fertilization strategy. This integration substantially improves PSNR (1.36 dB) and SSIM (0.0196), quantitatively validating our approach. Qualitatively, illustrated in Fig. 12 and compared between instances (f) and (c), (h) and (e), as well as (i) and (g), CZ-Net with the CIP module consistently yield sharper results than their module-less counterparts. This visually attests to the effectiveness of the CIP module within the CZ-Net framework.

5.4.2 Necessity of Loss Combination

From the absolute difference to the ground-truth sharp image and the metric performance (*i.e.*, PSNR \uparrow /SSIM \uparrow) shown in Fig. 13, we can observe that removing either \mathcal{L}_{esr} or \mathcal{L}_{att} leads to a degradation of the prediction of the results, indicating their contribution to restoring the sharp latent image. Specifically, \mathcal{L}_{esr} introduces the intra-frame information, *i.e.*, sharp texture, embedded in the HR event streams, which can guide the clearer details recovering for the MD task. \mathcal{L}_{att} provides blur-aware attention supervision to guide AAEs to alleviate the distortions embedded in the LR events and thus is also helpful in the entire MD task. Moreover, experiments are conducted to combine the above two loss functions to validate the effectiveness further. In general, Tab. 4 and Fig. 13 show that combining all these losses leads to the smallest absolute error, validating the necessity of recovering latent sharp images with \mathcal{L}_{esr} and \mathcal{L}_{att} simultaneously. Furthermore, through qualitative ablations of \mathcal{L}_{md} presented in Fig. 15, it becomes apparent that excluding the MD loss, \mathcal{L}_{md} , results in a deterioration in the HR events prediction, exemplified by the instance of the *wheel* in Fig. 15, indicating their contribution to furnish sharp details that aid in the recovery of HR event details.

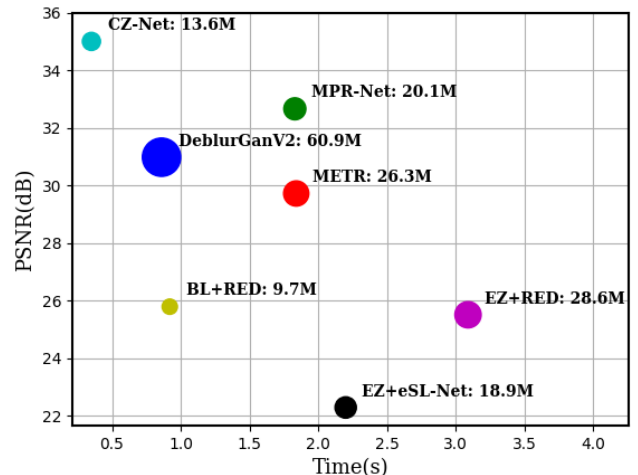


Fig. 16: Performance to complexity diagram on the GoPro dataset. The inference time is evaluated over the GoPro dataset by feeding blurry images of 640×360 , where the model in the top left corner has the highest efficiency and effectiveness. The size of the blobs is proportional to the number of network parameters.

5.5 Complexity to Performance Analysis

We further evaluate the complexity of our CZ-Net and SOTA MD and ESR methods on the synthetic GoPro dataset by feeding a blurry image with 640×360 and LR event stream with 160×90 and implementing them on an NVIDIA GeForce RTX 3090 GPU. The comparison results on the complexity-to-performance diagram are given in Fig. 16. Our CZ-Net achieves dominant performance in terms of PSNR (35.00 dB) but at the expense of the smallest time consumption (≈ 0.35 s), validating its superiority in efficiency and effectiveness. Furthermore, the model size regarding the number of parameters is also indicated in Fig. 16, where our CZ-Net is the second smallest network and has only 13.6 M parameters, validating its memory efficiency.

6 CONCLUSION

In this paper, we propose a novel CZ-Net to simultaneously achieve the sharp latent sequence restoration and the HR event stream reconstruction from a single blurry image and its concurrent LR event stream. Specifically, a multi-scale blur event fusion architecture is presented to achieve cross-enhancement by adequately utilizing scale-variant and fusing cross-modality data. Attention-based adaptive enhancement and cross-interaction prediction modules are designed to alleviate the coupled distortions embedded in LR events and reinforce the final results through the prior information. Furthermore, we proposed a hybrid system to build a new

dataset containing high-resolution, sharp sequences and the corresponding *real-world* LR event streams to narrow the real-to-synthetic gap. Extensive qualitative and quantitative experiments on synthetic and real-world datasets demonstrate that the proposed CZ-Net achieves state-of-the-art deblurring and event super-resolving performance.

REFERENCES

- [1] Siavash Arjomand Bigdeli, Matthias Zwicker, Paolo Favaro, and Meiguang Jin. Deep mean-shift priors for image restoration. *NeurIPS*, 30, 2017. **2**
- [2] Tony F. Chan and Chiu-Kwong Wong. Total variation blind deconvolution. *IEEE TIP*, 7(3):370–375, 1998. **2**
- [3] Liang Chen, Faming Fang, Tingting Wang, and Guixu Zhang. Blind image deblurring with local maximum gradient prior. In *CVPR*, pages 1742–1750, 2019. **2**
- [4] Sung Hyun Cho, Jue Wang, and Seungyong Lee. Handling outliers in non-blind image deconvolution. In *ICCV*, pages 495–502, 2011. **2**
- [5] Sung-Jin Cho, Seo-Won Ji, Jun-Pyo Hong, Seung-Won Jung, and Sung-Jea Ko. Rethinking coarse-to-fine approach in single image deblurring. In *CVPR*, pages 4641–4650, 2021. **2**
- [6] Jiangxin Dong, Jinshan Pan, Zhixun Su, and Ming-Hsuan Yang. Blind image deblurring with outlier handling. In *ICCV*, pages 2478–2486, 2017. **2**
- [7] Peiqi Duan, Zihao W Wang, Xinyu Zhou, Yi Ma, and Boxin Shi. Eventzoom: Learning to denoise and super resolve neuromorphic events. In *CVPR*, pages 12824–12833, 2021. **2, 3, 4, 7, 8**
- [8] Rob Fergus, Barun Singh, Aaron Hertzmann, Sam T. Roweis, and William T. Freeman. Removing camera shake from a single photograph. In *ACM SIGGRAPH*, pages 787–794, 2006. **2**
- [9] Martin A Fischler and Robert C Bolles. Random sample consensus: a paradigm for model fitting with applications to image analysis and automated cartography. *Communications of the ACM*, 24(6):381–395, 1981. **6**
- [10] Guillermo Gallego, Tobi Delbruck, Garrick Orchard, Chiara Bartolozzi, Brian Taba, Andrea Censi, Stefan Leutenegger, Andrew J. Davison, Jorg Conradt, Kostas Daniilidis, and Davide Scaramuzza. Event-based vision: A survey. *IEEE TPAMI*, 44(1):154–180, 2020. **1, 3**
- [11] Hongyun Gao, Xin Tao, Xiaoyong Shen, and Jiaya Jia. Dynamic scene deblurring with parameter selective sharing and nested skip connections. In *CVPR*, pages 3848–3856, 2019. **1, 2, 4**
- [12] Jin Han, Yixin Yang, Chu Zhou, Chao Xu, and Boxin Shi. Evntsnet: Event guided multiple latent frames reconstruction and super-resolution. In *ICCV*, pages 4882–4891, 2021. **1**
- [13] Chen Haoyu, Teng Minggui, Shi Boxin, Wang Yizhou, and Huang Tiejun. Learning to deblur and generate high frame rate video with an event camera. *arXiv preprint arXiv:2003.00847*, 2020. **3**
- [14] Zhewei Huang, Tianyuan Zhang, Wen Heng, Boxin Shi, and Shuchang Zhou. Real-time intermediate flow estimation for video frame interpolation. In *ECCV*, 2022. **6, 9**
- [15] Zhuangyi Jiang, Pengfei Xia, Kai Huang, Walter Stechele, Guang Chen, Zhenshan Bing, and Alois Knoll. Mixed frame-/event-driven fast pedestrian detection. In *ICRA*, pages 8332–8338, 2019. **1**
- [16] Yongcheng Jing, Yiding Yang, Xinchao Wang, Mingli Song, and Dacheng Tao. Turning frequency to resolution: Video super-resolution via event cameras. In *CVPR*, pages 7772–7781, 2021. **1**
- [17] Diederik P Kingma and Jimmy Ba. Adam: A method for stochastic optimization. In *ICLR*, 2015. **8**
- [18] Orest Kupyn, Volodymyr Budzan, Mykola Mykhailych, Dmytro Mishkin, and Jiri Matas. Deblurgan: Blind motion deblurring using conditional adversarial networks. In *CVPR*, pages 8183–8192, 2018. **2, 9**
- [19] Orest Kupyn, Tetiana Martyniuk, Junru Wu, and Zhangyang Wang. Deblurgan-v2: Deblurring (orders-of-magnitude) faster and better. In *ICCV*, pages 8878–8887, 2019. **7, 8**
- [20] Hongmin Li, Guoqi Li, and Luping Shi. Super-resolution of spatiotemporal event-stream image. *Neurocomputing*, 335:206–214, 2019. **3**
- [21] Zhen Li, Jinglei Yang, Zheng Liu, Xiaomin Yang, Gwanggil Jeon, and Wei Wu. Feedback network for image super-resolution. In *CVPR*, pages 3867–3876, 2019. **10, 11**
- [22] David G Lowe. Distinctive image features from scale-invariant keypoints. *IJCV*, 60(2):91–110, 2004. **6**
- [23] Tomer Michaeli and Michal Irani. Blind deblurring using internal patch recurrence. In *ECCV*, pages 783–798, 2014. **2**
- [24] Seungjun Nah, Tae Hyun Kim, and Kyoung Mu Lee. Deep multi-scale convolutional neural network for dynamic scene deblurring. In *CVPR*, pages 3883–3891, 2017. **2, 7**
- [25] Liyuan Pan, Richard Hartley, Cedric Scheerlinck, Miaomiao Liu, Xin Yu, and Yuchao Dai. High frame rate video reconstruction based on an event camera. *IEEE TPAMI*, 44(5):2519–2533, 2022. **2, 3**
- [26] Liyuan Pan, Cedric Scheerlinck, Xin Yu, Richard Hartley, Miaomiao Liu, and Yuchao Dai. Bringing a blurry frame alive at high frame-rate with an event camera. In *CVPR*, pages 6820–6829, 2019. **2, 3, 7**
- [27] Rui Qian, Robby T. Tan, Wenhan Yang, Jiajun Su, and Jiaying Liu. Attentive generative adversarial network for raindrop removal from a single image. In *CVPR*, pages 2482–2491, 2018. **5**
- [28] Henri Rebecq, Daniel Gehrig, and Davide Scaramuzza. Esim: an open event camera simulator. In *Conference on Robot Learning*, pages 969–982. PMLR, 2018. **7**
- [29] Henri Rebecq, René Ranftl, Vladlen Koltun, and Davide Scaramuzza. High speed and high dynamic range video with an event camera. *IEEE TPAMI*, 43(6):1964–1980, 2019. **11**
- [30] Uwe Schmidt, Carsten Rother, Sebastian Nowozin, Jeremy Jancsary, and Stefan Roth. Discriminative non-blind deblurring. In *CVPR*, pages 604–611, 2013. **2**
- [31] Chen Song, Qixing Huang, and Chandrajit Bajaj. E-cir: Event-enhanced continuous intensity recovery. In *CVPR*, pages 7803–7812, 2022. **7, 8**
- [32] Lei Sun, Christos Sakaridis, Jingyun Liang, Qi Jiang, Kailun Yang, Peng Sun, Yaozu Ye, Kaiwei Wang, and Luc Van Gool. Event-based fusion for motion deblurring with cross-modal attention. In *ECCV*, pages 412–428, 2022. **3, 7, 8**
- [33] Richard Szeliski. *Computer vision: algorithms and applications*. Springer Nature, 2022. **2**
- [34] Bishan Wang, Jingwei He, Lei Yu, Gui-Song Xia, and Wen Yang. Event enhanced high-quality image recovery. In *ECCV*, pages 155–171, 2020. **1, 7, 8**
- [35] Longguang Wang, Yingqian Wang, Xiaoyu Dong, Qingyu Xu, Jungang Yang, Wei An, and Yulan Guo. Unsupervised degradation representation learning for blind super-resolution. In *CVPR*, pages 10581–10590, 2021. **7, 8**
- [36] Zhou Wang, Alan C. Bovik, Hamid R. Sheikh, and Eero P. Simoncelli. Image quality assessment: from error visibility to structural similarity. *IEEE TIP*, 13(4):600–612, 2004. **7, 8**
- [37] Zihao W. Wang, Peiqi Duan, Oliver Cossairt, Aggelos Katsaggelos, Tiejun Huang, and Boxin Shi. Joint filtering of intensity images and neuromorphic events for high-resolution noise-robust imaging. In *CVPR*, pages 1609–1619, 2020. **1, 3, 4**
- [38] Wenming Weng, Yueyi Zhang, and Zhiwei Xiong. Boosting event stream super-resolution with a recurrent neural network. In *ECCV*, pages 470–488, 2022. **3, 4, 8, 10, 11**
- [39] Fang Xu, Lei Yu, Bishan Wang, Wen Yang, Gui-Song Xia, Xu Jia, Zhendong Qiao, and Jianzhuang Liu. Motion deblurring with real events. In *ICCV*, pages 2583–2592, 2021. **1, 2, 3, 7, 8**
- [40] Li Xu, Xin Tao, and Jiaya Jia. Inverse kernels for fast spatial deconvolution. In *ECCV*, pages 33–48, 2014. **2**
- [41] Zheng Xu, Liu Yexin, Lu Yunfan, Hua Tongyan, Pan Tianbo, Zhang Weiming, Tao Dacheng, and Wang Lin. Deep learning for event-based vision: A comprehensive survey and benchmarks. *arXiv preprint arXiv:2302.08890*, 2023. **1**
- [42] Syed Waqas Zamir, Aditya Arora, Salman Khan, Munawar Hayat, Fahad Shahbaz Khan, Ming-Hsuan Yang, and Ling Shao. Multi-stage progressive image restoration. In *CVPR*, 2021. **2, 7, 8, 9**
- [43] Xiang Zhang and Lei Yu. Unifying motion deblurring and frame interpolation with events. In *CVPR*, pages 17765–17774, 2022. **1, 3, 7**
- [44] Youjian Zhang, Chaoyue Wang, Stephen J. Maybank, and Dacheng Tao. Exposure trajectory recovery from motion blur. *IEEE TPAMI*, 44(11):7490–7504, 2021. **2, 7, 8, 9**
- [45] Junwei Zhao, Shiliang Zhang, and Tiejun Huang. Transformer-based domain adaptation for event data classification. In *ICASSP*, pages 4673–4677, 2022. **1**
- [46] Alex Zihao Zhu, Liangzhe Yuan, Kenneth Chaney, and Kostas Daniilidis. Unsupervised event-based optical flow using motion compensation. In *ECCV*, 2018. **4**